Wear mechanisms and friction parameters for sliding wear of micron-scale polysilicon sidewalls

D.H. Alsem [a,b,1], R. van der Hulst [c], E.A. Stach [d], M.T. Dugger [e], J.Th.M. De Hosson [c], R.O. Ritchie [a,f,*]

[a] Materials Sciences Division, Lawrence Berkeley National Laboratory, Berkeley, CA 94709, USA
[b] National Center for Electron Microscopy, Lawrence Berkeley National Laboratory, Berkeley, CA 94709, USA
[c] Department of Applied Physics, University of Groningen, Groningen, 9747 AG, The Netherlands
[d] Center for Functional Nanomaterials, Brookhaven National Laboratory, Upton, NY 11973, USA
[e] Materials Science and Engineering Center, Sandia National Laboratories, Albuquerque, NM 87185, USA
[f] Department of Materials Science and Engineering, University of California, Berkeley, CA 94720, USA

ARTICLE INFO

ABSTRACT

As tribological properties are critical factors in the reliability of silicon-based microelectromechanical systems, it is important to understand what governs wear and friction. Average dynamic friction, wear volumes and morphology have been studied for polysilicon devices fabricated using the Sandia SUMMiT V™ process and actuated in room-temperature air at μN loads. A total of seven devices was tested for total life. Three of the total-life experiments showed a global peak in the friction coefficient at three times the initial value with failure after 10^5 cycles. Four other total-life experiments ran similarly up to 10^5 cycles; however, following this global peak in the friction coefficient these devices continued to operate and achieved a lower steady-state friction regime with no failure for millions of cycles. Coincident with the friction coefficient increase, the nano-scale wear coefficient and surface roughness increased sharply in the first 10^5 cycles and then decayed over several million cycles. These results are considered in terms of a mechanistic understanding of wear and friction: after an initial short adhesive wear regime with early failures attributed to local spikes in friction caused by differences in the local nano-scale surface morphology, three-body abrasive wear becomes the governing mechanism, allowing the devices to achieve a steady-state friction regime. Changing the relative humidity, sliding speed and load in the steady-state regime, in which devices spend the majority of their operating life, is found to influence the friction coefficient, but re-oxidation of worn polysilicon surfaces was only found to have an effect on the friction coefficient after periods of inactivity.

© 2010 Elsevier B.V. All rights reserved.

1. Introduction

Microelectromechanical systems (MEMS) can be fabricated using low-cost batch processing and permit the miniaturization of many sensor and actuator applications [1,2]. Due to the large surface-to-volume ratio of these micrometer-sized structures, it is not always possible to simply extrapolate known macro-scale failure modes down to the micro- and nano-meter size-scales [3,4]. Although a growing body of research has provided insight into how to overcome problems in MEMS fabrication and design [2], premature failure modes – adhesion, wear and fatigue – are not well understood [4], which represents a challenge to the continued successful utilization of MEMS [5].

Adhesion [6,7] failures in MEMS are common in devices with contacting surfaces. Although several different solutions for this issue have been proposed, including critical-point drying procedures after release and the application of hydrophobic and/or low surface energy coatings (*e.g.*, Ashurst et al. [8–11]), this is still one of the major challenges with respect to MEMS reliability. Another reliability issue in MEMS is premature failure by fatigue; this is of particular interest in the case of micron-scale silicon, as large-scale specimens of silicon are not susceptible to cyclic fatigue fracture [12–18]. For all these failure modes, design approaches for MEMS reliability are largely empirical as mechanistic understanding has been limited by the simple fact that the physical mechanisms governing these processes for *thin-film* silicon are largely unknown. This is especially true for the problem of wear. Despite numerous published studies on the tribology of thin-film silicon, *e.g.* [6,19–29], the mechanistic aspects of wear are rarely the main focus. Consequently, there is currently no conclusive picture of what the prevailing physical mechanisms are that cause wear in thin-film silicon, although a few studies do provide some mechanistic insight. In early research on single-crystal sili-

---

* Corresponding author at: 216 Hearst Memorial Mining Building, University of California, Berkeley, CA 94720-1760, USA. Tel.: +1 510 486 5798; fax: +1 510 643 5792.
   E-mail address: RORitchie@lbl.gov (R.O. Ritchie).
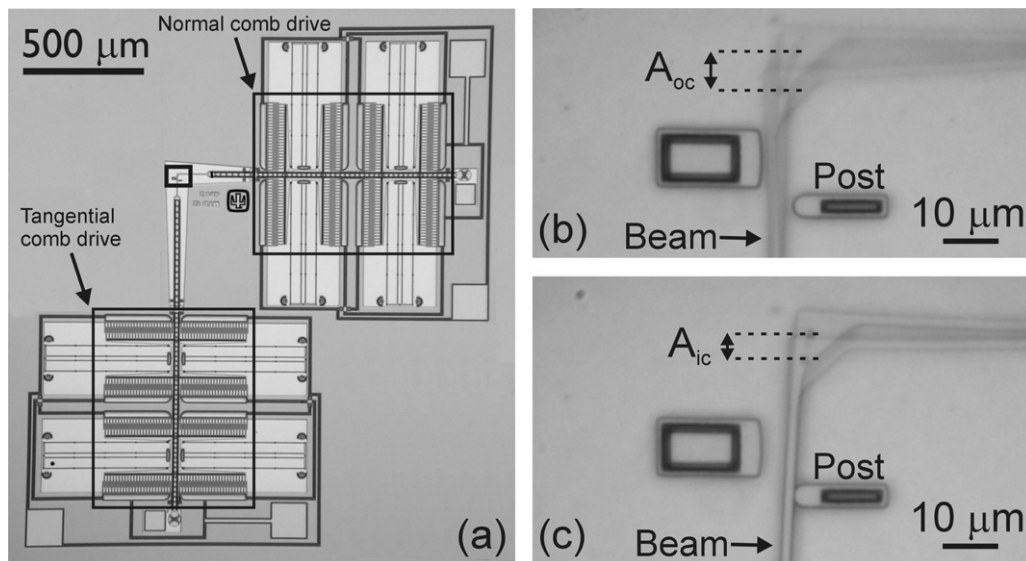[1] Now at Hummingbird Scientific, Lacey, WA, USA.

Fig. 1. (a) Optical micrographs showing an overview of a sidewall friction test device; the small rectangular mark is the region shown at higher magnification in (b) and (c), where the beam can be seen dynamically oscillating either out-of-contact with the post (b) or in contact with the post (c) – the blurring of the motion is caused by the reciprocal motion of the device.

con wafers, the wear mechanisms proposed were similar to those for bulk ceramics and metals, *i.e.*, abrasion, chipping and flattening of protrusions, plasticity and delamination wear [30–35]. Later studies on micro-fabricated surfaces [36,37] suggested a mechanism for single-crystal silicon of asperity contact/wear followed by atomistic-scale wear, whereas for polysilicon indirect morphological evidence of plasticity was claimed. Other researchers [38,39] have proposed that an adhesive wear mechanism could prevail. Specifically, during adhesive wear, asperities on two contacting surfaces adhere by plastic flow and cold-welding. Owing to continuing movement of these surfaces, fracture tends to occur away from the bonded interface leading to augmented asperities and wear debris, although no evidence of these processes was presented. Another study on wear in (dry) air [40–42] suggested that as the surface oxide layer wears, it regenerates resulting only in the wear of silicon dioxide. Finally, a recent study on micron-scale polycrystalline silicon [43] showed clear evidence of abrasive wear particles of amorphous SiO_2 after long sliding times; the smoothness of the majority of these particles was attributed to a polishing effect that occurred after the particles were initially created. Other than these multiple-asperity studies using MEMS contacts to specifically investigate the underlying mechanisms of wear, there is a sizable body of work that has applied atomic force and friction force microscopy, *e.g.* [44–47]. However, although these studies are extremely useful for gaining a basic understanding of friction and wear for single-asperity contacts, applying these insights to multi-asperity contacts in MEMS interfaces, where the exact contact morphology is hardly ever known, is not trivial. In addition, certain effects that have been reported in single-asperity contact studies, *e.g.*, super lubricity [48], have not been explicitly shown to be relevant in multi-asperity contact phenomena [29].

The lack of a comprehensive physical mechanistic description of wear and friction in micron-scale silicon multi-asperity contacts provides the rationale of the current work which is focused on polycrystalline silicon sidewalls. Our approach is to combine on-chip MEMS testing with atomic force and electron microscopy to examine wear debris and worn surfaces, coupled with quantitative measurements of the wear volume, surface roughness and the static and dynamic friction coefficients, to provide an underlying basis for the mechanisms that control wear and friction in

polysilicon at micrometer dimensions. In previous publications we have investigated wear debris by analytical transmission electron microscopy (TEM) [49] and measured static friction coefficients and scanning electron microscopy (SEM) surface morphology patterns as function of number of cycles, as well as wear volumes and surface roughness [50]. In this work we complement that work by also investigating how operating parameters affect friction when the surfaces have reached a steady-state friction regime. We measure the average dynamic coefficient of friction as function of wear cycles, investigate the influence of humidity and sliding speed on dynamic friction and use static friction coefficients to show the effect of contact pressure and re-oxidation on friction of polysilicon during wear in the steady-state friction regime in which these contacts will spend most of their operating lifetime. These results are compared with our previously acquired friction coefficient data and the polysilicon sidewalls morphology [49,50], and are discussed in terms of the physical mechanisms that we believe are active during micron-scale friction and wear processes.

2. Experimental methods

On-chip n$^+$-type polysilicon sidewall friction and wear test devices were fabricated using the Sandia SUMMiT V^{TM} fabrication process [51,52]. A 1H,1H,2H,2H-perflurordecyltrichlorosilane (PFTS) monolayer coating was deposited during release [53] to reduce unintentional adhesion of free-standing elements.[2] The device (Fig. 1) consists of two suspended shuttles, the normal and tangential shuttle (Fig. 1a). Each shuttle is driven laterally by an electrostatic comb drive (Fig. 1a). By applying a DC voltage to the normal comb drive, a beam is pushed against a post (Fig. 1b, c). Sinusoidal AC signals are applied to the tangential comb drive causing

---

[2] The coating was applied for ease of transport and handling, and released via the following steps in solution at room temperature: release etched (buffered HF), rinsed with DI water, oxidized with H_2O_2, rinsed with DI water, transferred to isopropyl alcohol and then to iso-octane, transferred to 1 mM solution of the monolayer in iso-octane and held in solution for 2 h, transferred to neat iso-octane, then to isopropyl alcohol and to DI water, before finally being removed from DI water and air dried on class 10 clean bench.

wearing of the beam against the post (Fig. 1b, c).[3] To determine the average normal force between the beam and the post during the wear process, the devices were calibrated by plotting the applied DC voltage in the normal comb drive and the bending of the beam up to when it touched the post; using elastic beam bending theory and the relation between applied voltage and force of the comb drive, the normal force can be determined as function of the applied voltage to the normal comb drive [10,50,55]. The average dynamic coefficient of friction ($\mu_d = F_{friction}/F_{normal}$) was determined, where $F_{friction}$ is the average dynamic friction force over 2–6 wear cycles and F_{normal} is the average applied normal force. While the latter is known from the calibration, the former was obtained by examining the difference between the maximum mechanical restoring force of the moving shuttle during dynamic cycling out-of-contact and dynamic cycling in-contact conditions, *i.e.*, by comparing the dynamic amplitude of the beam out-of-contact with the post, where $F_{friction} = 0$ (A_{oc}; as marked in Fig. 1b), and the dynamic amplitude in contact with the post, where $F_{friction} \neq 0$, (A_{ic}; as marked in Fig. 1c), which was measured by the distance between the center of a reference mark on the moving beam at the maximum and minimum deflection positions. The method for calculating the dynamic friction force is given in Appendix A; this gives the equation:

$$F_{friction} \approx \frac{1}{2}(A_{oc} - A_{ic}) \cdot (k'_b + k_c), \tag{1}$$

where k'_b is the effective spring constant of the normal beam and k_c is the effective spring constant of the folded beam shuttle suspension internal to the tangential comb drive [56]. The static coefficient of friction, μ_s, was measured by applying a normal load by means of a normal DC voltage and increasing the tangential force by ramping a second DC voltage signal (~1 V/s); the voltage was then noted where the beam first slips along the post, as observed through a 1000× optical microscope. A calibrated force balance of the beam touching the post was then used to obtain the value for the static coefficient of friction. More details on the calculations of the static coefficient of friction and the force calibration procedure can be found in Ref. [10].

The devices were operated at room temperature (23–27 °C) at a relative humidity (%RH) ranging from 10(±2%) to 90(±2%)% in a custom environmental chamber under a normal contact force of 1.5–3.7 μN at 100 Hz with sliding peak-to-peak amplitude of 4–6 μm (one wear cycle is equivalent to twice this distance)[4]; temperatures and %RH were measured using a digital thermometer/hygrometer. At these small scales, adhesive (*e.g.*, van der Waals, capillary and chemical) forces can be of the same order of magnitude as external forces. To account for these forces, an upper bound for the adhesion force with this contact geometry was determined by noting the difference in DC voltage when the beam and post are touching for the first and last time during the approach and upon separation. These voltages can be converted to forces using the comb drive calibration and subtracted from each other to give the adhesive force. This adhesion force was calculated to be ~0.2 μN. Since these forces appear an order of magnitude smaller than the applied normal force, we have not included them into the calculations for the coefficients of friction. The average device sliding velocity was deduced from the sliding amplitude and the frequency, which was first converted to the time it takes to slide through one complete cycle.

Scanning electron microscopy (SEM), using a JEOL 6340F microscope at 20 kV, was employed to image the overall wear mor-
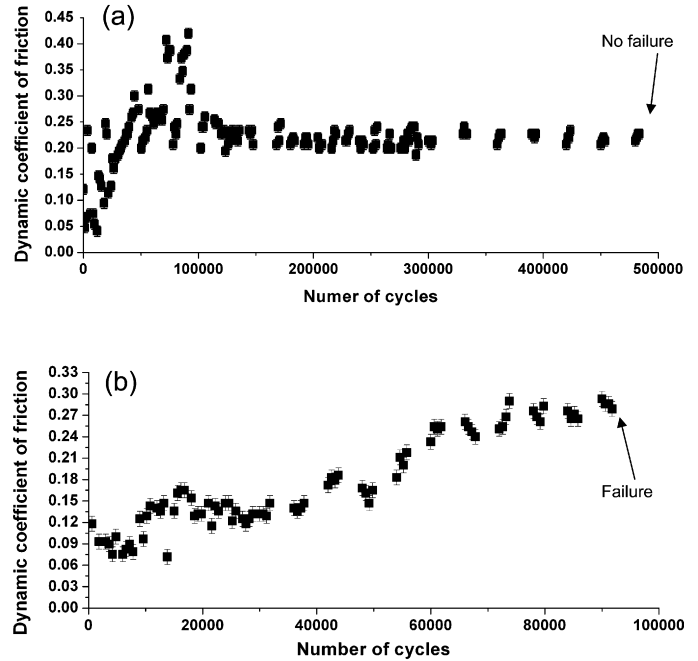
---

[3] Note that during the wear tests, the beam and post are not perfectly aligned; the beam is elevated somewhat with respect to the post due to comb-drive levitation effects [54].

[4] These were the operating conditions for all specimens, except those used to investigate the effect of sliding speed and normal load.

Fig. 2. (a) Example of results for the dynamic coefficient of friction as a function of number of cycles, for a device run at a normal force of 2.1 μN, showing no failure after 5×10^5 cycles after which the device was stopped. (b) Corresponding results of the dynamic coefficient of friction *vs.* number of cycles for a sidewall friction device that failed after ~10^5 cycles during the run-in phase (run at a normal force of 2.9 μN). The error bars are determined by the error of determining A_{oc} and A_{ic} as well as the error in the calibration.

phology. Atomic-force microscopy (AFM; Asylum Research MFP-3D in non-contact mode with a single crystal silicon tip) was used to determine nano-scale wear volumes and root-mean-square (*rms*) surface roughness after wearing to a certain number of cycles (the latter averaged over several ~4 μm² areas along the worn section of the beam); the site-specific sidewall AFM samples were prepared using a dual-beam focused ion beam system (FIB; FEI Strata DB235) equipped with a micromanipulator (Omniprobe™). Wear volumes were used to compute average dimensionless wear coefficients (k), using Archard's law [57,58]:

$$k = \frac{3HV_w}{SP} \tag{2}$$

where V_w is the worn volume (in m³), S is the total sliding length (in m), P is the normal load between the surfaces (in N), and H is the average material hardness (in Pa; 11.5 GPa for n⁺-type polysilicon films [46]). The wear coefficient represents the chance that a wear particle is generated from previously unworn silicon, and allows comparison of wear between experiments with differences in operating conditions. Further details on the AFM characterization are reported in Ref. [50].

3. Results

3.1. Friction

Two types of behavior were found during the measurements of the dynamic coefficient of friction as function of number of wear cycles in ambient air (31–41%RH), as shown in Fig. 2. Some devices were able to survive for millions of test cycles (where a cycle would vary from ~8 to 12 μm in sliding length depending on the operating parameters) (Fig. 2a), whereas others stopped functioning during a run-in phase after only ~10^5 cycles (Fig. 2b). A total of seven devices tested for total lifetime under similar operating conditions led to
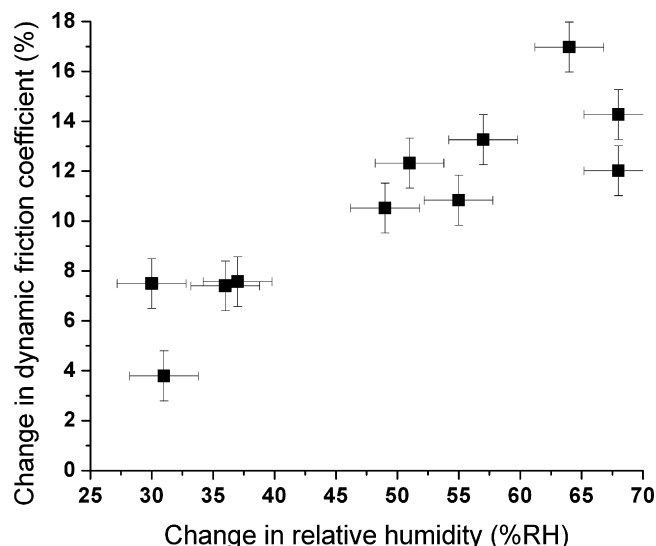
Fig. 3. Effect of relative humidity on the dynamic coefficient of friction in the steady-state friction coefficient regime, where a positive change indicates an increase in friction coefficient and %RH.

Fig. 4. Effect of sliding speed on the dynamic coefficient of friction in the steady-state friction coefficient regime (F_{normal} = 4.5 µN) in ambient air.

the observation of these two behavior modes [59]. Four devices ran for millions of cycles and reached a steady-state regime, while three ceased to operate after ~10^5 cycles in the run-in phase. Averaging over these devices, the initial dynamic coefficient of friction started at 0.10 ± 0.04 and reached a peak value during the run-in phase of 0.32 ± 0.10 at $1.0 \times 10^5 \pm 2 \times 10^4$ cycles. For the devices that did not cease motion at this peak value, the coefficient of friction subsequently decreased to reach a steady-state value of 0.25 ± 0.09. These values for the dynamic friction coefficient are comparable with those measured in other studies, which range from 0.1 to 0.5 [39,40,52,60]. It should be noted, however, that the lower-bound value in our work is the dynamic friction coefficient of the PFTS monolayer coating that is still present in the early stages of the wear process.

Once devices reached the steady-state region where they spend the majority of their lifetime (as observed in Fig. 2a), the parameters that influence the friction forces were investigated. These measurements provide quantitative insight into how operating parameters can affect the friction coefficient. First, the humidity inside the environmental chamber was increased from either an initial dry (~10%RH) or ambient air (~35%RH) up to humid air with a relative humidity larger than 60% (maximum humidity: 90%RH). The average change in friction coefficient due to the change in humidity was determined by averaging over ten or more friction data points at both humidity levels, after eliminating data points influenced by transition periods between different humidity conditions. Repeating this procedure several times at different start and finish humidity values and using three different devices yielded the cumulative results that are presented in Fig. 3. The absolute friction coefficients found in these experiments ranged from 0.30 to 0.10, depending on the history of the device and applied pressure, values that are largely consistent with those found in the steady-state regime for the total-life experiments.[5] These data show that with a larger increase in %RH, the dynamic friction coefficient also increased, suggesting that in the range tested here (10–90%RH),

higher relative humidity results in higher friction forces. Also note that within the humidity range of total lifetime testing of the friction coefficient as function of sliding cycles (Fig. 2), the spread in the %RH (31–41%) would only cause a 1–2% change in the average dynamic friction coefficient.

Another parameter that affects friction in the steady-state regime is sliding speed, which was also quantitatively measured by modifying the frequency of motion at constant dynamic amplitude. Fig. 4 shows a typical result of such experiments, where the data points are averaged from five or more dynamic coefficient of friction measurements in this regime. In the lower sliding speed regime below 1 mm/s (~100 Hz), a higher friction coefficient was measured, whereas at speeds greater than 3 mm/s (~300 Hz) the friction coefficients were all lower. In all experiments the transition from a higher friction to a lower friction regime happened at speeds between 1 and 3 mm/s, although the magnitude of the drop in friction coefficient, which varied between 10 and 30%, showed a less clear trend. This inconsistent decrease of the friction coefficient is most likely influenced by differences in normal loads, the humidity and the relative magnitude of the friction coefficient measured in individual experiments. It should be noted here that there are no effects of inertia when changing the speed, since the out-of-contact dynamic amplitude (A_{oc}, Fig. 1b) in the steady-state regime did not change when increasing the average sliding speed.

To examine the effect of normal load on static friction, the static coefficient of friction was determined as function of the normal load in the range of 1–20 µN. These measurements were taken after the devices had been stopped following operation in the steady-state friction regime (i.e., ≫10^5 cycles). Results are shown in Fig. 5 where every data point represents the average of four or more measurements. This experiment was repeated at several different times after the device was stopped; measurements revealed that after the cessation of cycling, some recovery of the surface occurred at loads above 2 µN, causing the friction coefficient to drop a factor of four after 168 h. This phenomenon is related to re-oxidation of the worn silicon surface which is initially not passivated by a silicon oxide layer once cycling is stopped. This was shown by running devices well into the steady-state regime (≫10^5 cycles); after cycling was stopped the static coefficient of friction was periodically measured. Fig. 6 shows that the static coefficient of friction stayed approximately constant for up to ~30 min after the device was stopped. Thereafter, it decreased over the next several thousand minutes

---

[5] The lower bound of these values was measured in devices that had been cycled for ≫2 million cycles. We noted a trend of a slight decrease in the friction coefficient in the steady-state friction regime (compare initial averages of 0.13 ± 0.05 with measured values down to 0.05 ≫2 million cycles), although this was not examined further.
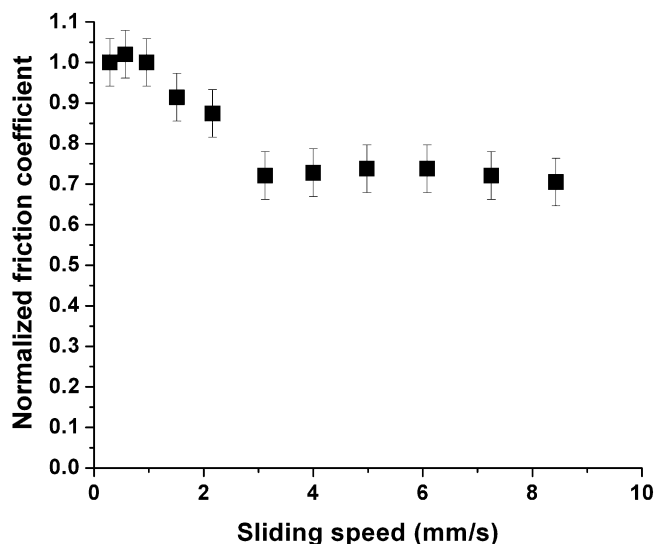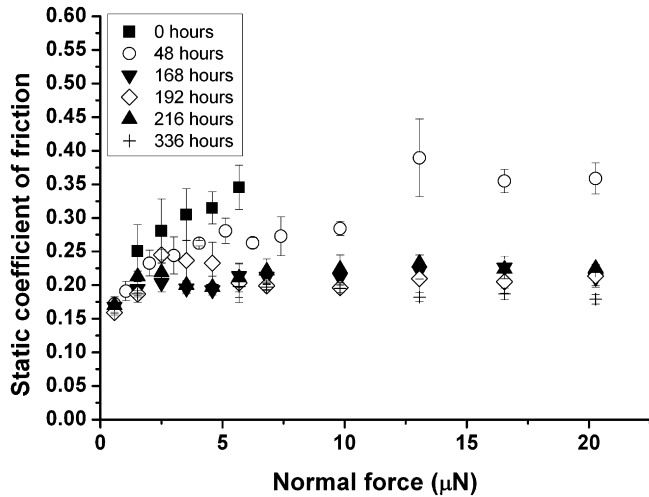
Fig. 5. Influence of normal force on the static friction coefficient as function of time in ambient air after stopping a wear test after the device has reached the steady-state regime.
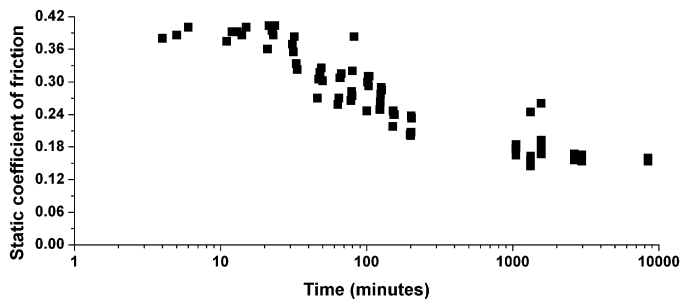

Fig. 6. Static coefficient of friction *vs.* idle time after a device has been subjected to wear for 7×10^5 cycles ($F_{normal} = 2.1 \, \mu N$).

before reaching a steady-state at a value approximately a factor of two lower than the maximum coefficient of friction and only slightly higher than the initial value, which is governed by the monolayer coating (0.12 ± 0.02 [50]) [59].

3.2. Wear morphology

To gain further insight into what governs whether a device ceases to move or continues to operate with a peak value of the

friction coefficient after $\sim 10^5$ cycles, SEM micrographs were taken of worn beams and posts. The surfaces of the beams and posts of devices are shown in Fig. 7. Images taken of devices that were running well in their steady-state regime (Fig. 7c, d) and after they failed at the peak of the friction coefficient during the run-in phase (Fig. 7a, b) indicate few differences in the overall surface morphology; in both cases abrasive wear grooves were observed on the beams with debris (agglomerates) present on both the beams and the posts.

A more quantitative picture of the wear patterns was obtained by examining the shape and depth of the grooves of the worn areas of the sidewall devices using AFM in order to measure nano-scale wear volumes and calculate wear coefficients (Fig. 8). Sources of error in the estimated value of the worn volume arise from the finite radius of the AFM tip (and its inability to reach the bottom of narrow grooves) and the fact that any wear of the post is not accounted for; however, the latter was essentially non-existent or at worst significantly smaller than the wear of the beam (Fig. 7) [50]. All these effects are included in the error bars for the wear coefficients in Fig. 8 [50]. The wear coefficients as well as the roughness, calculated from different devices as a function of wear cycles (Fig. 8), show that after an initial rise in the first $\sim 10^5$ cycles (to $\sim 10^{-4}$ and $\sim 40 \, nm$, respectively), both the wear coefficient and the roughness decay as the accumulated wear cycles increase (to respective values of $\sim 10^{-5}$ and $\sim 20 \, nm$) [50].

3.3. Contact stresses

Two different contact geometries were compared to make a rough estimate of the stresses that could occur during the wear and friction processes and to show the effect of the changes in the contact morphology on the stress state. The first was the geometry where the beam and post are in full contact, which represents a lower-bound contact stress value for these contacts; the second was the situation where a small wear particle gets trapped in between the surfaces of the beam and post, which represents an upper-bound contact stress value. A first-order approximation of the lower-bound stresses can be made by using the Hertzian contact theory of a cylinder on a flat [61] (Fig. 9a), where it is assumed that the beam can be considered a semi-infinite plate. Assuming contact along the entire thickness of the structural film, the contact width, $2a$, is given by:

$$2a = 2 \left(\frac{4 F_{normal} R_C}{\pi t E_C} \right)^{1/2} = 13 \, nm, \tag{3}$$
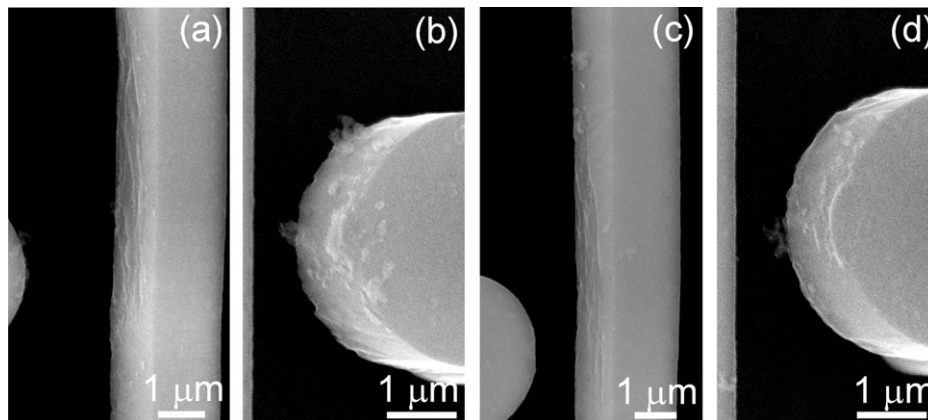
Fig. 7. SEM micrographs of: (a) device ($F_{normal} = 2.0 \, \mu N$) at the steady-state regime that was stopped after 7.5×10^5 cycles showing the beam (a) and the post (b); device ($F_{normal} = 2.9 \, \mu N$) that failed for a second time after 2.5×10^5 cycles (after already having failed at 10^5 cycles and being restarted) showing beam (c) and the post (d) – the second $\sim 1.5 \times 10^5$ cycles were run at a slightly higher tangential force to allow further cycling. All images are shown at 30° tilt and were taken at 20 keV. Note that the apparent bending of the beam is a charging artifact of the high-quality, slow scan speed images. After Ref. [59].
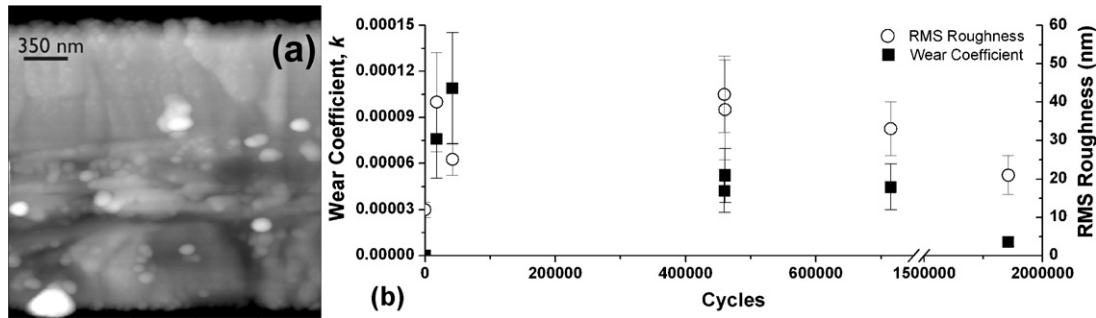
Fig. 8. (a) AFM scan of worn surface; gray-scale covers 250 nm. (b) Variation in the wear coefficient (squares) and *rms* roughness (circles) for polysilicon showing an initial rapid increase followed by a steady decrease with increasing number of wear cycles (normal contact forces ∼3–6 μN). After Ref. [50].

where F_{normal} is the normal force (3 μN), R_C is the radius of the post (2 μm), t is the film thickness (2.2 μm) and $E_C = E/2(1 − \nu^2)$; E (=163 GPa) and ν (=0.23) [62] are, respectively, the Young's modulus and Poisson's ratio of polysilicon. This gives a lower-bound contact stress of:

$$\sigma_{contact}^{min} = \frac{2F_{normal}}{\pi at} = 143 \text{ MPa}, \quad (4)$$

and a total contact area of $2at = 2.7 \times 10^{-2} \text{ μm}^2$. The upper-bound contact stress can be estimated by assuming that a small spherical debris particle is trapped between the beam and post (Fig. 9b), where in this case because of the small spherical size of the particle, both the beam and the post can be assumed to be semi-infinite, The contact radius, b, is then given by:

$$b = 2\left(\frac{3F_{normal}R_C}{4E_C}\right)^{1/3} = 8.7 \text{ nm}, \quad (5)$$

where R_C is the radius of the smallest observed particles during the studied wear processes (25 nm [49]), and the upper-bound contact stress is given by:

$$\sigma_{contact}^{max} = \frac{3F_{normal}}{2\pi b^2} = 19 \text{ GPa}, \quad (6)$$

with a total contact area of only $\pi b^2 = 4.8 \times 10^{-4} \text{ μm}^2$. Note that the latter calculated stress value is determined assuming that there is only elastic deformation without a yield criterion. Under these high compressive stress conditions this cannot be assumed; in nano-indentation of silicon it has been shown that the first non-linearity (associated with phase transformations) occurs at ∼10 GPa [63]. Therefore we use this value as the upper-bound stress for these contacts because no sub-surface plasticity or phase transformations were found in TEM cross-sections [49]. These calculations show that the contact stress can vary over about two orders of magnitude depending on which of the two local contact geometries shown in Fig. 9 dominates.
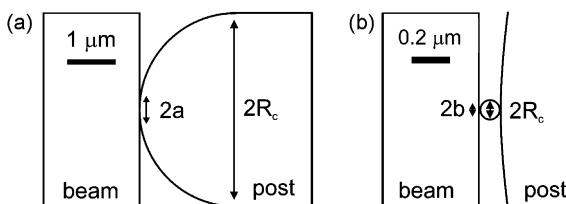

Fig. 9. Schematic of the beam and post contact geometry (top view) illustrating the lower-bound contact stress case (a), where the beam and post are fully in contact, and the upper-bound contact stress case (b), where a smallest observed individual wear particle is trapped between the surfaces.

4. Discussion

In this study of friction and wear of polysilicon structural films, the evolution of the micrometer-scale dynamic friction coefficients, wear coefficients, root-mean-square roughness and surface morphology has been measured as a function of the number of wear cycles. Additionally, the effect of parameters that affect the friction coefficient in the steady-state friction regime, specifically relative humidity, contact pressure and sliding speed, has also been investigated. These results are discussed below in terms of how they relate to the mechanistic processes that we believe occur during friction and micrometer-scale multi-asperity wear of polysilicon in room temperature air.

4.1. Dynamic friction coefficients and wear

The trend in the variation in the dynamic coefficient of friction for devices that survive past the run-in phase into the steady-state regime (Fig. 2a) shows a strong resemblance to the classical tribology theory [64,65]. In the classical case, abrasion between surface asperities leads to an initial increase in friction coefficient, and a steady-state friction coefficient is reached only when equilibrium is achieved between wear particle generation and particle fragmentation and ejection mechanisms. For the micron-scale case, we have previously shown that in the early stages of wear (<10^4 cycles) the monolayer coating and silicon-oxide are worn away by adhesive wear [50]. Consequently, some first silicon wear debris particles are generated after which the wear mechanism becomes abrasive wear. This transition in mechanism happens before the dynamic coefficient of friction, as well as the wear coefficient and surface roughness, reach their peak at ∼10^5 cycles near the end of the run-in phase (Figs. 2 and 8). The decrease in average wear coefficient after this peak indicates that as the number of cycles increases, there is a decreasing chance that new wear particles will be formed from unworn silicon (Fig. 8). Instead, previously formed wear particles interact between the contacting surfaces and break into smaller agglomerates, causing the *rms* roughness to decrease, as shown in Fig. 8. This is also consistent with recent results on a comparable study on wear of micron-scale polysilicon [43]. Past the run-in phase these changes result in an equilibrium steady-state friction regime (Fig. 2a), similar to classical tribological theory [64,65].

For devices that failed during the run-in phase at the peak in their friction coefficient (Fig. 2b), the initial development of the dynamic coefficient of friction is the same as for devices that did not fail (Fig. 2a); however, once the peak value of the friction coefficient was reached the former batch of devices ceased motion and failed (Fig. 2b). Because the detailed chemistry of the debris particles [50] and the global wear patterns look no different for these two distinct types of device behavior (Fig. 7), it appears that fail-

ure is governed by local variations in the friction coefficient caused by nano-meter scale variations in the contact morphology of the sidewall contacts. Wear particles that are trapped between these surfaces significantly lower the area of contact and hence the friction coefficient (compare the differences in contact area of the two configurations shown in Fig. 9a and b). However, at the same time these particles cause nano-scale ploughing which increases the friction coefficient, as shown by the absence of wear tracks in the early stages of wear [50] and presence of a multitude of abrasive tracks that is found in the later stages (Fig. 9). The interplay between these effects can cause local variations in the friction coefficient, which we cannot necessarily detect as our measurements of dynamic friction coefficients are averaged over a number of cycles. Other researchers though have measured these local spikes in friction coefficient for sliding for larger-scale contacts [66], and examined the influence of debris particles on the friction coefficient during macro-scale wear of silicon [35]. Moreover, our observations of two radically different failure behaviors of nominally identical polysilicon devices (Fig. 2) has also been recently observed for micron-scale wear of silicon in vacuum [67]. The prominent effect of such *local* nano-scale contacts on the tribological behavior is also apparent from the estimated lower- and upper-bound contact stresses for the two different geometries (Fig. 9). In the case, where the apparent contact area dominates (Fig. 9a), the contact stresses would only be ~143 MPa, whereas if local wear debris particle contacts are paramount (Fig. 9b), the contact stresses would be more than two orders of magnitude higher, *i.e.*, ~10 GPa. In our previous work [49,50], we showed that the governing mechanism for wear of thin-film silicon is an abrasive wear mechanism and that this mechanism is controlled by fracture. As fracture stresses for polysilicon are in the range 0.5–5 GPa [68], in order for fracture to control the abrasion process, stresses in the GPa range would needed, and this could only occur when debris particles between the surface govern device behavior. This indicates that the value of the friction coefficient, the failure point and the wear mechanism (*i.e.*, the abrasive nano-scale ploughing) are governed by (variations in) the local nano-scale contact morphology. However, it should be noted that despite the fact that the measured trends in friction forces and post-mortem surface/debris characterization are all consistent with the mechanisms described above, it remains difficult to know exactly which processes occur at the sliding interfaces because a lack of knowledge of the exact contact morphology.

4.2. Friction parameter: humidity, load and sliding speed

The data in Fig. 3 indicate that a larger change in humidity is associated with a larger change in the friction coefficient, an observation that could be explained by the presence of a thin layer of water molecules on the wearing surfaces in room temperature air. As the humidity rises (at constant temperature), more water molecules adhere to the beam, post and debris particle surfaces (*i.e.*, the surface water coverage increases [69,70]) and because of the relatively low sliding speeds and relatively low loads, this can significantly increase the friction force when the presence of additional water molecules on the surface causes additional adhesive (*e.g.*, polar, capillary) forces. A similar increase was observed by other researchers using both MEMS contacts and AFM [71,72]. A systematic quantitative study on the increase of capillary adhesion alone [73] showed that this component of the friction force rises exponentially with increase in the humidity, which would explain why an increase in a presumed minor component of the dynamic friction coefficient (*i.e.*, the friction forces caused by capillary adhesion) can measurably change the dynamic coefficient of friction.

The effect of load on the dynamic friction force is quantified in Fig. 5, which indicates that there is an increase in the friction coefficient when the load is raised from 1 to 5 µN. When the load passes 5 µN, a plateau is reached in the value of the friction coefficient (Fig. 5). One of the reasons that the friction coefficient can initially increase is the larger real area of contact between the surfaces from elastic deformation of the initial points of contact as the load is increased. At higher loads (>5 µN), many additional points of contact can form, such that the stresses on all the contacts are essentially constant with further elevation in load; this in turn prevents further increases in the real area of contact and hence the friction coefficient. This plateau at higher loads could indicate that at first contact (≥ 1 µN) there are only a few local points of contact and it is not until significantly higher loads (>5 µN) that more contacts are formed, which provides a further indication of the importance of the local contacts on the overall behavior of the sliding interfaces. Note that although the load clearly has an influence on the friction coefficient in the steady-state regime (Fig. 5), it was not possible to correlate slightly different loads during total life testing to the two distinct types of failure behavior shown in Fig. 2.

The influence of load on static friction also depends on how long a device is stopped after cycling (Fig. 5). The effect of time after cessation of device operation is quantified in Fig. 6, where the decay of the static coefficient of friction after stopping a worn device in the steady-state regime is shown. This is attributed to re-growth of the native oxide layer that was removed during the wear process [49]. Studies of native SiO_2 growth on single crystal silicon shows a constantly increasing growth [74] that continues beyond the testing time shown in Fig. 6. This would indicate that the first 30 min of native oxide growth on the worn surface following cessation of motion does not affect the static friction force measurably, and that because the friction force reaches a lower plateau after 10^3–10^4 min, further growth of the SiO_2 layer has no additional effect on the friction coefficient either. The data in Fig. 6 also suggest that re-oxidation does not affect the friction forces measurably during sliding, since a long time of inactivity is needed before the effect can be seen. This would suggest a minimal influence, if any, of re-oxidation of the worn surface during the wear process, in contrast to previously published work in which re-oxidation of the silicon surface was used to describe the salient wear mechanism in ambient air [42]. The lack of influence of re-oxidation is consistent with the fact that the smallest wear particles found that were not agglomerates were on the order of 50–100 nm [49], *i.e.* larger than the thickness of the oxide layer.

Finally, the effect of sliding speed on the friction coefficient (Fig. 4) shows that at low sliding speeds the friction coefficient appears to be smaller than at higher speeds, with the transition in this particular case happening between 1 and 3 mm/s. We attribute this to a higher contribution of the adhesion force due to chemical bonding or capillary condensation on the surface, which also contributes to the fact that the static friction coefficient is higher than the dynamic coefficient of friction [75]. At these low sliding speeds, which can be compared to quasi-static sliding, this adhesive force, which is not accounted for in the calculation of the normal force, can still measurably affect the value of the friction coefficient (Fig. 5).

4.3. Wear mechanisms

The effects of the different friction parameters on the friction coefficients (Figs. 2–6 and 8) that have been observed in this study were physically explained within the framework of a dominant three-body abrasive wear mechanism active during sliding wear of polysilicon. These trends, combined with our previous work on this topic, where we showed the surface evolution and static friction coefficient as function of the number of wear cycles and a detailed TEM study of the surface and wear debris [49,50], form the basis for our proposed mechanism for wear of thin-film polysilicon under µN loads in ambient

air. The sliding wear process initially comprises adhesive wear during the run-in phase, where the monolayer coating and the silicon oxide wears away (in $\sim 5 \times 10^3$ cycles) [50]. The removal of these layers creates freshly exposed silicon surfaces on the beam and post, which then can come into contact to form strong chemical bonds (similar to the configuration shown in Fig. 9a). The wear mechanism then transitions to adhesive wear of the silicon itself, during which the friction coefficient slowly increases; this involves the creation of adhesive wear debris by fracture of the surface silicon grains, specifically from the sliding beam [50]. As soon as a critical mass of wear particles has been generated – which happens in a relative early stage of the wear process ($<10^4$ cycles) during the run-in phase – the governing wear mechanism changes from adhesive to mostly (third-body) abrasive wear (prior to the steady-state value of the friction coefficient being reached) [50], corresponding to the geometry shown in Fig. 9b. In this abrasive wear regime, wear grooves are created on the surface by the removal of more debris particles (50–100 nm with agglomerates up to ~ 500 nm [49]), where the removal is predominantly governed by fracture through the grains (~ 430 nm [18]) [49] and not by plasticity or cold-welding, as suggested in previous studies [38,39]. After the friction and wear coefficients and the surface roughness reach their peaks (Figs. 2, 8), the friction coefficient decays into the steady-state regime, where the device will spend most of its operating lifetime; in this regime, existing wear particle agglomerates are slowly broken down into smaller agglomerates, leading to a lower roughness (Fig. 8). The wear debris particles oxidize heavily and amorphize, and as such evolve into amorphous SiO_x particles [49]. Indeed, the existence of such amorphous stoichiometric SiO_2 as wear debris in micron-scale wear of polysilicon MEMS was recently reported [43]. All of these processes are controlled by fracture and not by plastic deformation of the silicon, since no evidence of plasticity was found in TEM cross-section specimens of the wear tracks [49]. Re-oxidation of the worn silicon surfaces (Fig. 6) and fatigue (Fig. 8) also do not appear to be factors in the wear process. The measured trends in the wear coefficients (Fig. 8) clearly imply that the creation of the initial wear particles is not controlled by fatigue. Although both micron-scale silicon [12–18] and silicon dioxide (glass) [76,77] have been shown to be susceptible to environmentally-assisted subcritical cracking and fatigue has been suggested as a contributor to wear in studies of macro-scale ceramics [34], it is not very likely that this mechanism plays a dominant role in the processes studied in this work. If this were the case, the trend in wear coefficient (Fig. 8) would be expected to increase as the number of sliding cycles increases and the majority of the debris would be created after longer cycling, which is simply not seen (Fig. 7). However, it is conceivable that fatigue cracking could aid in the break-up and polishing of newly created heavily oxidized debris particles.

For these types of devices with sidewalls in sliding contact, all these physical processes in the abrasive regime are controlled by the local contact morphology, which also determines the failure point (as opposed to the active wear mechanism, which is similar in both type of device behavior (Figs. 2, 7)). This can be deduced from the bi-modal failure behavior that these devices display (Fig. 2) and the similarity in the wear mechanisms found for both types of failures (Fig. 7). The quantitative tribological data presented in this study are fully consistent with these wear mechanisms. These additional details regarding the friction and wear processes and the effect of variations of friction parameters strengthen the argument for the proposed mechanisms of wear of polysilicon in ambient air.

Finally, it has to be noted that despite careful post-mortem characterization of the surfaces, it remains difficult to be conclusive on all the exact details of the proposed wear processes *as they are occurring* because of a lack of knowledge of the exact multi-asperity contact interface. Future *in situ* electron microscopy studies, *e.g.* [78,79], may be enabling here by providing details on the exact morphology of the multi-asperity contacts.

5. Summary and conclusions

On-chip n+-type polysilicon MEMS sidewall friction devices have been used to study dynamic friction, wear volumes and the morphology of polycrystalline silicon run in ambient air at μN normal loads. Measurements of the dynamic coefficient of friction during the wear process were correlated with SEM images of worn surfaces, AFM measurements determining the *rms* surface roughness and corresponding evolution of the average wear coefficient. Additionally, the effects of operating parameters (humidity, normal load and sliding speed) on the coefficient of friction were investigated in the steady-state regime, in which the devices spend most of their lifetime. All these data were combined into wear mechanisms for micron-scale polysilicon.

The wear process begins with the removal of the hydrophobic coating and silicon oxide by adhesive wear ($<5 \times 10^3$ cycles, where each cycle represents a sliding distance of ~ 10 μm), after which the coefficient of friction increases to a peak value of 0.3 ± 0.1 at $\sim 10^5$ cycles during the run-in phase. During these first 10^5 cycles, a transition from adhesive wear to (three-body) abrasive wear occurs before $\sim 10^4$ cycles, the latter being the dominant wear mechanisms for most of the lifetime of the devices. Some devices are able to cycle for millions of cycles after reaching a slightly lower steady-state coefficient of friction of 0.25 ± 0.10 after $>10^5$ cycles, while other devices stop functioning at the peak in the friction coefficient due to an increasing friction force during the run-in phase. Whether a device fails early or not is governed by local variations in the friction force, caused by local variations in surface morphology. In the steady-state regime, the friction force increases with relative humidity because of additional polar and capillary forces due to the thicker adsorbed water layers on the surface. Additionally, load and sliding speed also influence the friction coefficient in this regime. With respect to sliding speed, slower sliding speeds (<1 mm/s) result in higher friction coefficients whereas speeds above ~ 3 mm/s result in lower friction coefficients, an effect that can be related to the chemical bonding force between the surfaces. Increasing the contact load from 1 to 5 μN causes the friction coefficient to increase, although further load increases (up to 20 μN) have little effect; this is related to the evolution of the contact area and the number of contact points as the load in increased. It was found that re-oxidation of polysilicon only has a significant influence on the coefficient of static friction some 30 min after the device has stopped, further indicating that oxide re-growth does not influence wear during cycling. These results are consistent with a proposed mechanism for ambient-temperature wear of thin-film polycrystalline silicon which involves a predominantly (three-body) abrasive wear mechanism controlled by the local contact geometry of particles between the sliding surfaces.

the U.S. Department of Energy's National Nuclear Security Administration under contract DE-AC04-94AL85000.

Appendix A. Calculation of the dynamic friction force

The dynamic friction force is determined from the difference between the out-of-contact and in-contact amplitude; the equations of motion in the in- and out-of contact scenario (as shown in Fig. 1) can be written:

Out-of-contact:

$$F_{comb} = ma_{oc} + bv_{oc} + x_{oc}(k'_b + k_c), \tag{A1}$$

In-contact:

$$F_{comb} = ma_{ic} + bv_{ic} + x_{ic}\left(k'_b + k_c\right) + F_{friction}, \tag{A2}$$

where F_{comb} is the electrostatic force produced by the comb drive, m the mass of the shuttle, b the damping coefficient, k'_b is the effective spring constant of the normal beam, and k_c is the effective spring constant of the folded beam shuttle suspension internal to the tangential comb drive. Since the force from the comb drive is equal in both scenarios, these two equations can be combined as:

$$ma_{oc} + bv_{oc} + x_{oc}\left(k'_b + k_c\right) = ma_{ic} + bv_{ic} + x_{ic}\left(k'_b + k_c\right) + F_{friction}, \tag{A3}$$

or rearranged to:

$$m\left(a_{oc} - a_{ic}\right) + b\left(v_{oc} - v_{ic}\right) + \left(x_{oc} - x_{ic}\right)\left(k'_b + k_c\right) = F_{friction}. \tag{A4}$$

The dynamic friction force can then be calculated by observing the case of $x = (1/2)A$, $v = 0$ for both the in- and out-of-contact scenarios. This yields:

$$m\left(a_{oc} - a_{ic}\right) + 1/2\left(A_{oc} - A_{ic}\right)\left(k'_b + k_c\right) = F_{friction}. \tag{A5}$$

With respect to this equation (Eq. (A5)), we can readily show that $m\left(a_{oc} - a_{ic}\right) \ll 1/2\left(A_{oc} - A_{ic}\right)\left(k'_b + k_c\right)$. The difference in acceleration between the in- and out-of-contact scenarios can be written as $a_{oc} - a_{ic} = 2(\pi f)^2 \left(A_{oc} - A_{ic}\right)$. Since the device is cycling at 100 Hz and the difference in amplitude $(A_{oc} - A_{ic})$ in these experiments is typically about 1.5 μm, this makes the value of $a_{oc} - a_{ic}$ approximately 0.3. Although it is difficult to determine the exact mass of the system, a rough estimate of the mass based on the two-dimensional area of the shuttle comes out to $\sim 5 \times 10^{-10}$ kg, implying that the term $m(a_{oc} - a_{ic})$ in Eq. (A5) is on the order of 2×10^{-10} N.

The term $\left(k'_b + k_c\right)$ can be determined using a similar calibration procedure to that of the normal comb drive (described in Ref. [10]); its value lies between 0 and 1 N/m, implying that the friction force is in the 10^{-7} N range. Therefore, we can express the final relationship for the dynamic friction coefficient as:

$$F_{friction} \approx 1/2(A_{oc} - A_{ic}) \cdot (k'_b + k_c)$$

Note that we have taken a conservative approach to the dynamic friction force by taking the maximum value during a cycle. This was done because seizure of the device during cycling is determined by the highest friction force encountered.

Error bars in the friction coefficient values were computed from the error in the measurement of A_{ic} and A_{oc} and the error from the comb drive calibration, the latter containing all the imperfections from the linear elastic comb drive spring model [10] and device-to-device geometric variations.

References

[1] B. Bhushan, H.W. Liu, Characterization of nanomechanical and nanotribological properties of digital micromirror devices, Nanotechnology 15 (2004) 1785.

[2] N. Maluf, K. Williams, An Introduction to Microelectromechanical Systems Engineering, Artech House Publishers, Boston, 2004.

[3] K. Komvopoulos, Surface engineering and microtribology for micromechanical systems, Wear 200 (1996) 305–327.

[4] A.D. Romig, M.T. Dugger, P.J. McWhorter, Materials issues in microelectromechanical devices: science, engineering, manufacturability and reliability, Acta Materialia 51 (2003) 5837–5866.

[5] C. Fung, Industry study on issues of MEMS reliability and accelerated lifetime testing, in: IEEE 43th International Reliability Physics Symposium, 2005, p. 312.

[6] S.H. Kim, D.B. Asay, M.T. Dugger, Nanotribology and MEMS, Nano Today 2 (2007) 22–29.

[7] R. Maboudian, W.R. Ashurst, C. Carraro, Tribological challenges in microelectromechanical systems, Tribology Letters 12 (2002) 95–100.

[8] W.R. Ashurst, C. Carraro, R. Maboudian, Vapor phase anti-stiction coatings for MEMS, IEEE Transactions on Device and Materials Reliability 3 (2003) 173–178.

[9] W.R. Ashurst, M.B.J. Wijesundara, C. Carraro, R. Maboudian, Tribological impact of sic encapsulation of released polycrystalline silicon microstructures, Tribology Letters 17 (2004) 195–198.

[10] W.R. Ashurst, C. Yau, C. Carraro, R. Maboudian, M.T. Dugger, Dichlorodimethylsilane as an anti-stiction monolayer for MEMS: a comparison to the octadecyltrichlosilane self-assembled monolayer, Journal of Microelectromechanical Systems 10 (2001) 41–49.

[11] M.P. de Boer, D.L. Luck, W.R. Ashurst, R. Maboudian, A.D. Corwin, J.A. Walraven, J.M. Redmond, High-performance surface-micromachined inchworm actuator, Journal of Microelectromechanical Systems 13 (2004) 63–74.

[12] D.H. Alsem, C.L. Muhlstein, E.A. Stach, R.O. Ritchie, Further considerations on high-cycle fatigue of micron-scale polycrystalline silicon, Scripta Materialia 59 (2008) 931–935.

[13] D.H. Alsem, O.N. Pierron, E.A. Stach, C.L. Muhlstein, R.O. Ritchie, Mechanisms for fatigue of micron-scale silicon structural films, Advanced Engineering Materials 9 (2007) 15–30.

[14] D.H. Alsem, E.A. Stach, C.L. Muhlstein, R.O. Ritchie, Fatigue failure in thin-film polycrystalline silicon is due to subcritical cracking within the oxide layer, Applied Physics Letters 86 (2005), 041914-1-3.

[15] D.H. Alsem, R. Timmerman, B.L. Boyce, E.A. Stach, J.T.M. De Hosson, R.O. Ritchie, Very high-cycle fatigue failure in micron-scale polycrystalline silicon films: effects of environment and surface oxide thickness, Journal of Applied Physics 101 (2007), 013515-1-9.

[16] H. Kahn, R. Ballarini, A.H. Heuer, Dynamic fatigue of silicon, Current Opinion in Solid State & Materials Science 8 (2004) 71–76.

[17] C.L. Muhlstein, E.A. Stach, R.O. Ritchie, A reaction-layer mechanism for the delayed failure of micron-scale polycrystalline silicon structural films subjected to high-cycle fatigue loading, Acta Materialia 50 (2002) 3579–3595.

[18] D.H. Alsem, B.L. Boyce, E.A. Stach, R.O. Ritchie, Effect of post-release sidewall morphology on the fracture and fatigue properties of polycrystalline silicon structural films, Sensors and Actuators A 147 (2008) 553–560.

[19] Q. Chen, G.P. Carman, Microscale tribology (friction) measurement and influence of crystal orientation and fabrication process, in: Proc. 13th Annual Inter. Conf. on Micro Electro Mechanical Systems, 2000, pp. 657–661.

[20] E.E. Flater, A.D. Corwin, M.P. De Boer, R.W. Carpick, In situ wear studies of surface micromachined interfaces subject to controlled loading, Wear 260 (2006) 580–593.

[21] D.A. Hook, S.J. Timpe, M.T. Dugger, J. Krim, Tribological degradation of fluorocarbon coated silicon microdevice surfaces in normal and sliding contact, Journal of Applied Physics 104 (2008), 034303-1-3.

[22] A. Lumbantobing, K. Komvopoulos, Static friction in polysilicon surface micromachines, Journal of Microelectromechanical Systems 14 (2005) 651–663.

[23] G. Subhash, A.D. Corwin, M.P. De Boer, Operational wear and friction in MEMS devices, in: Proc. 11th International Conference on Fracture, 2005.

[24] N.R. Tas, C. Gui, M. Elwenspoek, Static friction in elastic adhesive MEMS contacts, models, and experiment, in: Proc. 13th Annual Inter. Conf. on Micro Electro Mechanical Systems, 2000, pp. 193–198.

[25] S.J. Timpe, K. Komvopoulos, M.T. Dugger, Microscale friction phenomena in oscillatory sliding contacts, Journal of Applied Physics 102 (2007), 123503-1-8.

[26] W.M. Van Spengen, J.W.M. Frenken, The Leiden MEMS tribometer: real time dynamic friction loop measurements with an on-chip tribometer, Tribology Letters 28 (2007) 149–156.

[27] W. Wang, Y. Wang, H. Bao, B. Xiong, M. Bao, Friction and wear properties in MEMS, Sensors and Actuators A 97–98 (2002) 486–491.

[28] J.A. Williams, H.R. Le, Tribology and MEMS, Journal of Physics D: Applied Physics 39 (2006) R201–R214.

[29] J. Wu, S. Wang, J. Miao, A MEMS device for studying the friction behavior of micromachined sidewall surfaces, Journal of Microelectromechanical Systems 17 (2008) 921–933.

[30] R.G. Bayer, Influence of oxygen on the wear of silicon, Wear 69 (1981) 235–239.

[31] S. Danyluk, J.L. Clark, The wear rate of n-type Si (1 0 0), Wear 103 (1985) 149–159.

[32] S. Danyluk, R. Reaves, Influence of fluids on the abrasion of silicon by diamond, Wear 77 (1982) 81–87.

[33] D.E. Kim, N.P. Suh, On microscopic mechanisms of friction and wear, Wear 149 (1991) 199–208.

[34] T.E. Fischer, Z. Zhu, H. Kim, D.S. Shin, Genesis and role of wear debris in sliding wear of ceramics, Wear 245 (2000) 53–60.

[35] E. Zanoria, S. Danyluk, M. McNallan, Effects of length, diameter and population density of tribological rolls on friction between self-mated silicon, Wear 181–183 (1995) 784–789.

[36] U. Beerschwinger, T. Albrecht, D. Mathieson, R.L. Reuben, S.J. Yang, M. Taghizadeh, Wear at microscopic scales and light loads for MEMS applications, Wear 181 (1995) 426–435.

[37] U. Beerschwinger, R. Mathieson, R.L. Reuben, S.J. Yang, A study of wear on MEMS contact morphologies, Journal of Micromechanics and Microengineering 4 (1994) 95–105.

[38] D.M. Tanner, W.M. Miller, W.P. Eaton, L.W. Irwin, K.A. Peterson, M.T. Dugger, D.C. Senft, N.F. Smith, P. Tangyunyong, S.L. Miller, IEEE International Reliability Physics Symposium Proceedings 26–35 (1998).

[39] D.M. Tanner, J.A. Walraven, L.W. Irwin, M.T. Dugger, N.F. Smith, W.P. Eaton, W.M. Miller, S.L. Miller, The effect of humidity on the reliability of a surface micromachined microengine, IEEE International Reliability Physics Symposium (1999) 189–197.

[40] S.T. Patton, W.D. Cowan, K.C. Eapen, J.S. Zabinski, Effect of surface chemistry on the tribological performance of a MEMS electrostatic lateral output motor, Tribology International 9 (2000) 199–209.

[41] S.T. Patton, W.D. Cowan, J.S. Zabinski, Performance and reliability of a new MEMS electrostatic lateral output motor, in: 37th Annual International Reliability Physics Symposium, 1999, pp. 179–188.

[42] S.T. Patton, J.S. Zabinski, Failure mechanisms of a MEMS actuator in very high vacuum, Tribology International 15 (2002) 373–379.

[43] D.S. Grierson, A.R. Konicek, G.E. Wabiszewski, A.V. Sumant, M.P. de Boer, A.D. Corwin, R.W. Carpick, Characterization of microscale wear in a polysilicon-based MEMS device using AFM and PEEM–NEXAFS spectromicroscopy, Tribology Letters 36 (2009) 233–238.

[44] B. Bhushan, Nano- to microscale wear and mechanical characterization using scanning probe microscopy, Wear 251 (2001) 1105–1123.

[45] B. Bhushan, V.N. Koinkar, Microtribological studies of doped single-crystal silicon and polysilicon films for MEMS devices, Sensors and Actuators A 57 (1996) 91–102.

[46] B. Bhushan, X. Li, Micromechanical and tribological characterization of doped single-crystal silicon and polysilicon films for microelectromechanical systems devices, Journal of Materials Research 12 (1997) 54–63.

[47] R.W. Carpick, M. Salmeron, Scratching the surface: fundamental investigations of tribology with atomic force microscopy, Chemical Reviews 97 (1997) 1163–1194.

[48] A. Socoliuc, R. Bennewitz, E. Gnecco, E. Meyer, Transition from stick-slip to continuous sliding in atomic friction: entering a new regime of ultralow friction, Physical Review Letters 92 (2004), 134301/1-4.

[49] D.H. Alsem, E.A. Stach, M.T. Dugger, M. Enachescu, R.O. Ritchie, An electron microscopy study of wear in polysilicon microelectromechanical systems in ambient air, Thin Solid Films 515 (2007) 3259–3266.

[50] D.H. Alsem, M.T. Dugger, E.A. Stach, R.O. Ritchie, Micron-scale friction and sliding wear of polycrystalline silicon thin structural films in ambient air, Journal of Microelectromechanical Systems 17 (2008) 1144–1154.

[51] More information available at: http://mems.sandia.gov.

[52] D.C. Senft, M.T. Dugger, Friction and wear in surface micromachined tribological test devices, in: Proc. SPIE Micromachined Devices and Components III, 1997, pp. 31–38.

[53] U. Srinivasan, M.R. Houston, R.T. Howe, R. Maboudian, Alkyltrichlorosilane-based self-assembled monolayer films for stiction reduction in silicon micromachines, Journal of Microelectromechanical Systems 7 (1998) 252–260.

[54] W.C. Tang, M.G. Lim, R.T. Howe, Electrostatic comb drive levitation and control method, Journal of Microelectromechanical Systems 1 (1992) 170.

[55] J.J. Sniegowski, E.J. Garcia, Microfabricated actuators and their application to optics, Miniaturized Systems with Micro-Optics and Micromechanics 2383 (1995) 46.

[56] S.J. Timpe, K. Komvopoulos, Microdevice for measuring friction and adhesion properties of sidewall contact interfaces of microelectromechanical systems, Review of Scientific Instruments 78 (2007), 065106-1-9.

[57] J.F. Archard, Contact and rubbing of flat surfaces, Journal of Applied Physics 24 (1953) 981–988.

[58] J.F. Archard, Single contacts and multiple encounters, Journal of Applied Physics 32 (1961) 1420.

[59] D.H. Alsem, R. Van der Hulst, E.A. Stach, M.T. Dugger, J.T.M. De Hosson, R.O. Ritchie, Nano-scale tribological behavior of polycrystalline silicon structural films in ambient air, in: Proceedings of the MRS Spring Meeting, 2008.

[60] S.T. Patton, J.S. Zabinski, Advanced tribometer for in situ studies of friction, wear, and contact condition—advanced tribometer for friction and wear studies, Tribology Letters 13 (2002) 263–273.

[61] K.L Johnson, Contact Mechanics, Cambridge University Press, Cambridge, UK, 1987.

[62] G. Simmons, H. Wang, Single Crystal Elastic Constants and Calculated Aggregate Properties: A Handbook, M.I.T. Press, Cambridge, MA, 1971.

[63] J.E. Bradby, J.S. Williams, J. Wong-Leung, M.V. Swain, P. Munroe, Transmission electron microscopy observation of deformation microstructure under spherical indentation in silicon, Applied Physics Letters 77 (2000) 3749–3751.

[64] N.P. Suh, Tribophysics, Prentice-Hall, Englewood Cliffs, NJ, 1986.

[65] N.P. Suh, H.C. Sin, The genesis of friction, Wear 69 (1981) 91–114.

[66] S. Kurzenhauser, V. Hegadekatte, J. Schneider, N. Huber, O. Kraft, K.-H. Zum Gahr, Tribological characterization and numerical wear simulation of micro-components under sliding and rolling conditions, Microsystem Technologies 14 (2008) 1839–1846.

[67] S.J. Timpe, D.H. Alsem, D.A. Hook, M.T. Dugger, K. Komvopoulos, Wear of polysilicon surface micromachines operated in high vacuum, Journal of Microelectromechanical Systems 18 (2008) 229–238.

[68] O.M. Jadaan, N.N. Nemeth, J. Bagdahn, W.N. Sharpe, Probabilistic Weibull behavior and mechanical properties of MEMS brittle materials, Journal of Materials Science 38 (2003) 4087–4113.

[69] S. Brunauer, L.S. Deming, W.E. Deming, E. Teller, On a theory of the Van der Waals adsorption of gases, Journal of the American Chemical Society 62 (1940) 1723–1732.

[70] S. Brunauer, P.H. Emmett, E. Teller, Adsorption of gases in multimolecular layers, Journal of the American Chemical Society 60 (1938) 309–319.

[71] V.N. Koinkar, B. Bhushan, Microtribological studies of unlubricated and lubricated surfaces using atomic force friction force microscopy, Journal of Vacuum Science & Technology A-Vacuum Surfaces and Films 14 (1996) 2378–2391.

[72] D.M. Tanner, M.T. Dugger, Wear mechanisms in a reliability methodology, Reliability, Testing, and Characterization of MEMS/MOEMS II 4980 (2003) 22–40.

[73] M.P. De Boer, Capillary adhesion between elastically hard rough surfaces, Experimental Mechanics 47 (2007) 171–183.

[74] W.B. Ying, Y. Mizokawa, Y. Kamiura, K. Kawamoto, W.Y. Yang, The chemical composition changes of silicon and phosphorus in the process of native oxide formation of heavily phosphorus doped silicon, Applied Surface Science 181 (2001) 1–14.

[75] E. Rabinowicz, The nature of the static and kinetic coefficients of friction, Journal of Applied Physics 22 (1951) 1373–1379.

[76] S.M. Wiederhorn, Crack growth as an interpretation of static fatigue, Journal of Non-Crystalline Solids 19 (1975) 169–181.

[77] S.M. Wiederhorn, A chemical interpretation of static fatigue, Journal of the American Ceramic Society 55 (1972) 81–85.

[78] R. Ribeiro, Z. Shan, A.M. Minor, H. Liang, In situ observation of nano-abrasive wear, Wear 263 (2007) 1556–1559.

[79] A.P. Merkle, L.D. Marks, Friction in full view, Applied Physics Letters 90 (2007), 064101-1-3.

Biographies

Daan Hein Alsem received his PhD degree in Materials Science and Engineering from the University of California, Berkeley in 2006. After a post-doc in the Materials Sciences Division and the National Center for Electron Microscopy at the Lawrence Berkeley National Laboratory he is now the Director of Research at Hummingbird Scientific. His primary research interests are mechanical behavior of thin films, nanomaterials and novel structural materials as well as the application of new *in-situ* (analytical) transmission electron microscopy characterization methods.

Ruben van der Hulst received his MS degree in Applied Physics at the University of Groningen, the Netherlands. His work is focused on tribological behavior of thin films and coatings.

Eric A. Stach is a Scientist at the Center for Functional Nanomaterials at Brookhaven National Laboratory. He is also an Adjunct Professor of Materials Engineering at Purdue University, where he formally was a Professor. He received his PhD from the University of Virginia in 1998. After that he was Principal Investigator and Program Leader within the Materials Science Division and the National Center for Electron Microscopy at the Lawrence Berkeley National Laboratory. Dr. Stach's research focuses on the development and application of advanced electron microscopy techniques for the real time observation of nanostructured crystal growth and nanomaterials reliability.

Michael T. Dugger received his PhD in Materials Science and Engineering from Northwestern University in 1990. He is currently a Distinguished Member of the Technical Staff at Sandia National Laboratories in Albuquerque, New Mexico, where he conducts a wide range of fundamental to applied research in tribology. Research topics include friction and wear in microelectromechanical systems (MEMS), vapor phase lubrication, friction and wear in hard coatings, aging and performance of solid lubricants, particle generation due to wear, and the relationship between mechanical and electrical behavior of electrical contacts.

Jeff Th.M. De Hosson received his degrees in physics from University of Utrecht (BSc, MSc) and University of Groningen (1975, PhD), the Netherlands. He is currently Professor Applied Physics at the University of Groningen and the Chair of the Applied Science Division of the Royal Netherlands Academy of Sciences. His research efforts concentrate on studies of the dynamical behavior of defects in materials through in situ electron microscopy. He was elected to the Royal Holland Society of Sciences and Humanities in 1996 and the Royal Netherlands Academy of Sciences in 2000.

Robert O. Ritchie received the B.A. degree in physics and metallurgy, and the M.S, PhD, and Sc.D. degrees in materials science from Cambridge University, Cambridge U.K., in 1969, 1973, 1973 and 1990, respectively. He is currently the H.T. & Jessie Chua Distinguished Professor of Engineering and the Chair of the Materials Science and Engineering Department,University of California, Berkeley, and Senior Faculty Scientist with the Materials Sciences Division, Lawrence Berkeley National Laboratory, Berkeley. His primary research interest is the mechanical behavior of engineering and biological materials. Dr. Ritchie is a member of the National Academy of Engineering and the U.K. Royal Academy of Engineering.